Isotope Specific Kinetics of Hydroxyl Radical (OH) with Water (H₂O): Testing Models of Reactivity and Atmospheric Fractionation

Manvendra K. Dubey,* Ralf Mohrschladt,[†] Neil M. Donahue, and James G. Anderson

Department of Chemistry, Harvard University, Cambridge, Massachusetts 02138

Received: July 31, 1996; In Final Form: December 6, 1996[⊗]

Gas-phase hydrogen (H) abstractions from molecules by free radicals have been studied extensively. They form the simplest class of elementary reactions and also play a key role in atmospheric chemistry and so are the centerpiece of models of reactivity. Despite intense scrutiny, two fundamental mechanistic issues remain unresolved: (1) Do H abstractions proceed directly or indirectly? (2) Do thermodynamic or electronic interactions determine their reaction barrier? The thermoneutral identity reaction, $OH + H_2O \rightarrow H_2O + OH$, provides an excellent opportunity to answer these questions. Several theoretically predicted H_2O-HO complexes raise the possibility of an indirect mechanism, while no thermodynamic forcing influences the reaction barrier. To examine the various reactivity models, the isotopic scrambling reactions $^{18}OH + H_2^{16}O \rightarrow H_2^{18}O + ^{16}OH$ and $^{16}OD + H_2^{16}O \rightarrow H^{16}OD + ^{16}OH$ are studied in a high-pressure flow reactor. The measured rate constants are $(2.3 \pm 1.0) \times 10^{-13} \exp[-(2100 \pm 250)/T]$ cm³ molecule⁻¹ s⁻¹ over the range 300−420 K $((2.2 \pm 1.0) \times 10^{-16}$ at 300 K) and $(3 \pm 1.0) \times 10^{-16}$ cm³ molecule⁻¹ s⁻¹ at 300 K, respectively. The similarity between the room temperature rates indicates a small secondary isotope effect. While the strong temperature dependence reveals that the predicted complexes do not stabilize the isotope exchange transition state sufficiently to bring its energy below the reactants, the small preexponential factor indicates that the complexes pose entropic constraints. Therefore, the reaction mechanism appears to be indirect. This is clarified by tracing the evolution of reagent electronic interactions and geometrical transformations along the reaction path. Activation energies of isotope exchange reactions are used to constrain the thermoneutral intercept for themodynamically based reactivity models. These thermochemical models are shown to be unreliable. However, a correlation between theoretical (*ab initio*) and experimental reaction barriers does capture gross reactivity trends. These measurements also exclude kinetic fractionation by OH as an important contributor to the isotopic fractionation of water in the earth's atmosphere.

I. Introduction

The mechanism of the elementary gas-phase radical−molecule identity reaction,

$$HO + HOH \rightarrow (OH-HOH)^* \rightarrow HOH + OH \quad (1)$$

can be investigated by measuring the kinetics of associated isotope exchange reactions,

$$H^{18}O + HOH \rightarrow (^{18}OH-HOH)^* \rightarrow H^{18}OH + OH \quad (2)$$

$$DO + HOH \rightarrow (OD-HOH)^* \rightarrow HOD + OH \quad (3)$$

Each of these reactions may proceed directly to products or indirectly through a relatively stable intermediate, as indicated. Kinetics measurements of reaction 1 will be blind to all but the complex formation channel, while measurements of reactions 2 and 3 will be sensitive to both complex and product formation.

Identity reactions like (1) are thermoneutral and proceed over a symmetric electronic potential energy surface. Therefore, their transition state energies are determined principally by electronic (exchange, coulomb, charge transfer, and polarization) interactions.[1] Thermochemical reactivity models[2] are based on the premise that reaction enthalpy governs reaction barrier heights. They prescribe a function relating barrier height to reaction enthalpy that includes an intercept at thermoneutrality; this

"intrinsic" barrier is not described by the theory and thus must be constrained by other means, such as experimental measurements of isotope exchange processes like reactions 2 and 3. Our objective is to test the predictive power of these models by comparing them with both observations and *ab initio* calculations. Our broader goal is to resolve whether overall reaction energetics or electronic interactions at the transition state control reactivity of H abstraction reactions.

The premise of using reaction 1 as a basis for a predictive model of H atom abstractions is that this reaction is direct. However, *ab initio* calculations predict several H_2O-HO complexes, including a global minimum at an O−H separation of 2 Å that is bound by 5.7 kcal/mol.[3] The morphology of the potential energy surface along the reaction coordinate qualitatively depicted in Figure 1 has an isomerization barrier inside a relatively deep well. The overall behavior of reactions 1−3 will depend critically on whether the barrier to isotope exchange lies above or below the energy of the separated reagents. If the complex suppresses the energy of the H atom exchange transition state below the energy of the reactants, the reaction could proceed indirectly. In this case the overall rate of reactions 2 and 3 will be determined by entropic constraints at the transition state. Consequently, the reactions should be moderately fast, with a negative activation energy and possibly a pressure dependence (as is observed for the *termolecular* reactions of OH with H,[4] NO, and NO₂.[5−7]). If the transition state energy lies above the reactants, the reactions would display more "normal" *bimolecular* behavior. In this case reactions 2 and 3 should be slow, with a positive activation energy and no pressure dependence.[6,8]

---
* Corresponding author now at Molecular Physics Laboratory, SRI International, 333 Ravenswood Avenue, Menlo Park, CA 94025. Email: dubey@mplvax.sri.com.
[†] Now at BASF, Germany.
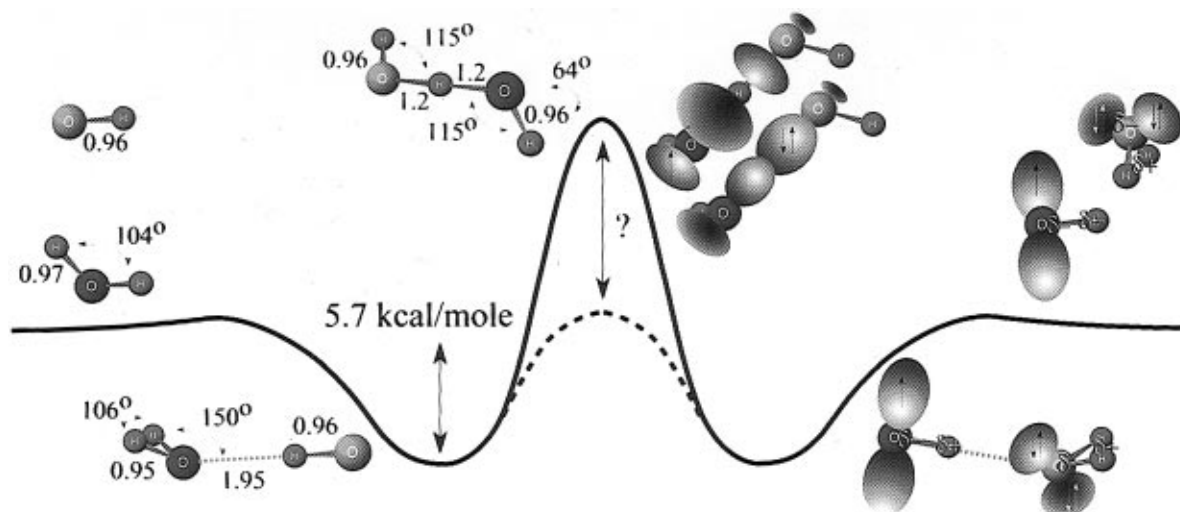[⊗] Abstract published in *Advance ACS Abstracts,* February 1, 1997.

Kinetics of Hydroxyl Radical with Water

J. Phys. Chem. A, Vol. 101, No. 8, 1997 **1495**

Figure 1. Minimum-energy path and electronic interactions. A schematic of the symmetric minimum-energy path of the HO + HOH → HOH + OH reaction is shown. The surface depicts the global minimum (of the many local minima) for the OH−OH$_2$ complex as well as the transition state for H atom transfer. The transition state may be higher (solid line) or lower (dash line) in energy than the reagents, depending on the extent that the long-range forces stabilizing the complex are preserved and augmented by short-range interactions. We expect slow H atom exchange for the high barrier while fast H atom transfer for the barrierless case. Optimized configurations (UHF//6-31G**) of the reactants, complex, and transition state are shown on the left side of the transition state. The evolution of electrostatic and orbital interactions as the reagents transform to the complex and then the transition sate is presented on the right. Dark and light shades indicate the phase of the molecular orbitals. Dipoles are indicated by δ^+ and δ^- on the reactants and complex. The complex is stabilized by dipolar attractions and bonding interactions from delocalizing the lone pair on O in the HOH molecule toward OH. The transition state is stabilized by the net interaction of the SOMO of the HO radical with an inner shell H−O σ bonding orbital in HOH. We measure the H atom transfer rate by isotopically labeling either an oxygen atom (as shown in the figure with different shades of blue) or a terminal hydrogen. In this work we demonstrate that this reaction is slow (high barrier) and show that a complex interplay of dipolar, frontier orbital, and reactive orbital interactions governs the reaction path.

The isotope exchange reactions 2 and 3 could also play a role in the earth's atmosphere. Current schemes to infer earth's paleotemperatures from the isotopic composition of ancient precipitation (e.g., ice core) consider the equilibrium vapor pressure isotope effect of water to be the exclusive source of isotopic fractionation. They neglect the possibility that various isotopes of water can react with atmospheric OH with different rate constants to effect the isotopic composition of water. If these reactions were moderately fast and had sufficiently different rate constants, they would provide a kinetic isotope fractionation mechanism for atmospheric water vapor. For example, kinetic fractionations are important in determining the isotopic composition of atmospheric methane[9] and of carbon monoxide in the lower Antarctic stratosphere.[10] We shall test the validity of omitting the kinetic isotope effect in paleotemperature inversion algorithms with our results.

II. Experimental Technique and Results

The high-pressure flow reactor, data acquisition, and analysis techniques used in the kinetic studies are discussed in detail elsewhere.[12,13] The key elements of the method are summarized here. In our closed-loop system the center of a fully developed flow of N$_2$ is seeded with OH radicals 50 cm upstream of an 80 cm long reaction zone. The OH radicals are produced by titrating F atoms generated in a high-pressure microwave discharge of F$_2$ in Ar with H$_2$O carried by He

$$F + H_2O \rightarrow OH + HF \qquad (4)$$

We produce the isotopes ^{18}OH and OD by changing the H$_2$O in the source to H$_2^{18}$O and D$_2$O, respectively. In the reaction zone the core of the OH plume is probed at five equidistant axial positions by laser-induced fluorescence (LIF) before it encounters the wall. Reaction time is determined by measuring the core flow velocity with a Pitot tube situated just downstream of the reaction zone; while a correction is applied for radial

diffusion, the effect is very small.[13] Reaction temperature is controlled by heating the tube walls upstream of the reaction zone. The temperature is measured with a thermistor mounted to the Pitot tube. It is stable to within 2 K throughout the reaction zone.

We use a tunable dye laser to pump a specific rovibronic OH transition near 282 nm, generally the Q$_1$(2) rotational line in the A$^2\Sigma^+$(v=1) ← X$^2\Pi$(v=0) electronic band. The LIF is measured at 309 nm by PMTs mounted orthogonal to the excitation beam. The laser is etalon narrowed (0.1 cm^{-1} peak width), ensuring isotopic specific detection of OH. A single laser beam passes through all five LIF axes, thus eliminating any errors due to laser power fluctuation. Using as a guide the high-resolution spectra for the (00) and (11) vibrational bands of A ← X excitation for ^{18}OH, together with rovibronic constants,[11] we observe the Λ doublets of the Q$_1$(2) for ^{18}OH, red-shifted by 10 cm^{-1} relative to ^{16}OH (282 nm). Analogously, the A$^2\Sigma^+$(v=1) ← X$^2\Pi$(v=0) transition is observed close to 287 nm for OD.

After we verify that the OH source is stable and the OH plume in the system is in a steady state, liquid H$_2$O is injected into the core of the flow with a syringe through a septum located 10.5 m upstream of the reaction zone. This allows sufficient time for evaporation and uniform mixing of H$_2$O. Chemical reaction causes fractional destruction of OH (^{18}OH or OD) radicals in the core of the flow proportional to both the H$_2$O concentration and reaction time (distance down the tube). These OH decays are monitored at the multiple LIF axes as the H$_2$O abundance gradually declines due to the continuous replenishment of carrier gas in the HPF system. (Approximately 5% of the recirculating flow is exchanged on each circuit through the system.) We measure H$_2$O directly by absorption of the 184.9 nm Hg line over a 7 m length in the return path of the flow tube, using the recommended H$_2$O cross section (5.5 × 10^{-20} cm^2 at 184.9 nm).[14] There is some indication that the true cross section may be up to 25% higher.[15] If this is borne out, and if

a similar error exists in the D_2O cross section, the rate constants reported here will be uniformly increased by about 25%. The time evolution of the UV absorption signal for a typical run at 20 Torr is displayed in Figure 2a.

The signal at the downstream axes (2–5) is divided by that at axis 1 to eliminate any effect of laser power fluctuations, OH source drifts, or quenching caused by the excess reagent (H_2O). To extract the rate constant, we first plot the logarithm of the normalized OH signal at each axis as a function of H_2O concentration[13] (e.g., Figure 2b). We find the slope of each of these lines, which eliminates any axis specific calibration constants. These normalized OH decays are then plotted against axis number, the surrogate for time, and the bimolecular rate constant determined from the slope (e.g., Figure 2c). The system stability and short time between experiments allow rapid study of multiple reactions. A calibration run of the reaction of OH with ethane is coupled with all our measurements for validation.

The very slow reactions under study pose several experimental challenges, which the high-pressure flow system is well-suited to meet. Large H_2O concentrations (1–2 Torr) are required to force sufficient OH decay. These H_2O levels could perturb the flow and will reduce the OH fluorescence signal by increasing quenching. Perturbations to the flow are minimized by performing kinetic studies at high pressures (>20 Torr). These H_2O levels cause substantial quenching of the OH fluorescence; however, the quenching is identical for all the LIF axes and is removed by normalizing the signal at all axes by that at axis 1.

Impurities in the H_2O would almost certainly lead to loss of both ^{16}OH and ^{18}OH. Therefore, reaction 1 is used as null. Investigations of reaction 1 revealed no OH decays even upon addition of a large excess (3 Torr) of H_2O, demonstrating the absence of impurities in the H_2O, as well as negligible OH loss from $H_2O–HO$ complex formation under the experimental conditions (room temperature and pressures less than 40 Torr). This null run is performed prior to all isotope exchange measurements.

The time evolution of UV absorption by H_2O for a typical run at 20 Torr is displayed in Figure 2a. The logarithm of the normalized ^{18}OH decays observed at each axis after H_2O addition are plotted against the H_2O concentration in Figure 2b. The linear decays in Figure 2b indicate that the experiment is free of additional OH sources or sinks, other than the title reaction. These decays at each axis are plotted as a function of axis number, which is proportional to reaction time, in Figure 2c. The slope of this linear plot is scaled by the measured velocity to determine the bimolecular rate constant.

We performed 14 such measurements of reaction 2 at 300 K at different pressures (5–40 Torr) and report a pressure-independent rate constant of $(2.2 \pm 1.0) \times 10^{-16}$ cm^3 molecule^{-1} s^{-1}. We also monitored the OH generated by reaction 2 by tuning the laser to ^{16}OH. While this production is clearly resolvable, extraction of an accurate rate is hampered because of the presence of a background of OH in the system. We estimate that OH production from (2) occurs at a rate faster than 2×10^{-17} cm^3 molecule^{-1} s^{-1} at 300 K qualitatively consistent with measurements of the ^{18}OH decays.

We have also measured the temperature dependence of the rate constant of reaction 2 from 300 to 420 K.[16] The Arrhenius plot shown in Figure 3 is fitted to get a preexponential factor of $(2.3 \pm 1.0) \times 10^{-13}$ cm^3 molecule^{-1} s^{-1} and an activation energy of 4.2 ± 0.5 kcal mol^{-1}.

The study of reaction 3 is performed by detecting OD by an excitation that is about 5 nm red-shifted from OH. Linear OD
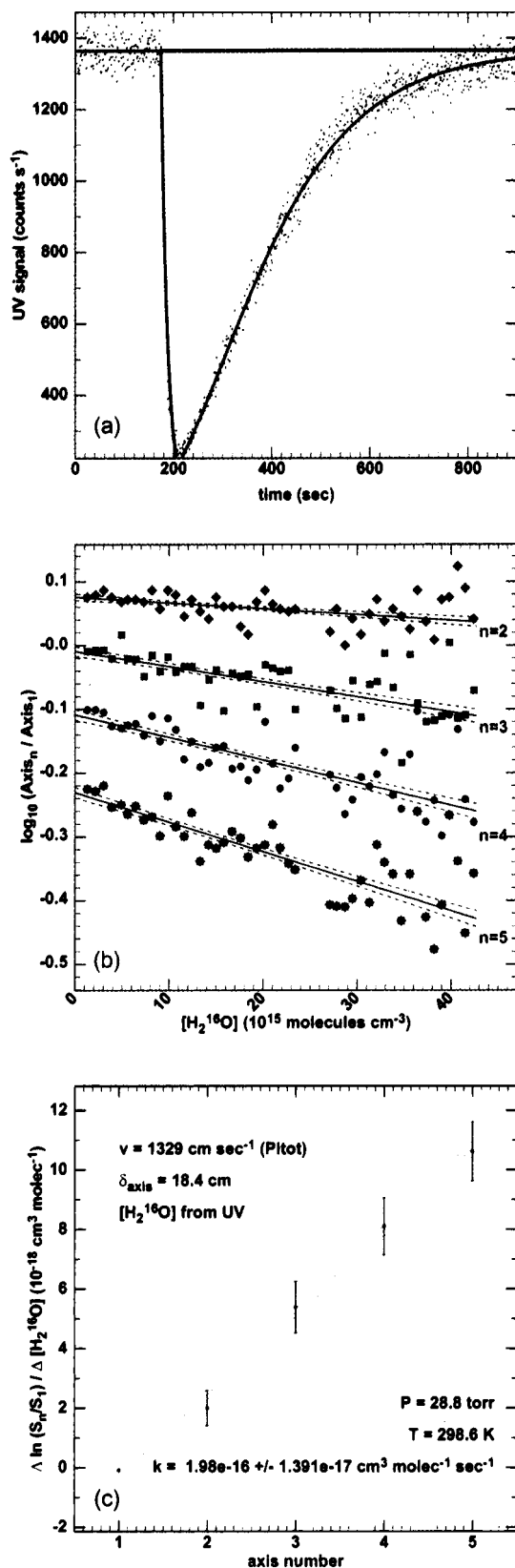

Figure 2. Data analysis to extract rate constant. (a) UV signal vs time. UV signal after absorption by H_2O of the 184.9 nm Hg line along a 7 m return path. The initial steep drop in the signal is caused by rapid injection of a pulse of water 180 s into a typical 15 min kinetics run. Water is gradually reduced by evacuation along with continuous replenishment of 5% of the recirculating flow with nitrogen leading to the continuous decay of the absorption signal. (b) $\log(S_{axis\ i/axis\ 1})$ vs H_2O. Normalized LIF signal for axis 2–5 of ^{18}OH as a function of H_2O concentration derived from the UV absorption signal. (c) Decays at each axis vs axis number. Variation of the slopes of $\log(S_{axis\ i/axis\ 1})$ vs H_2O plot for individual axis (from Figure 2) with axis number. The nominal zero slope for axis 1 is included. The slope of this plot is multiplied by the measured velocity to get the bimolecular rate coefficient.
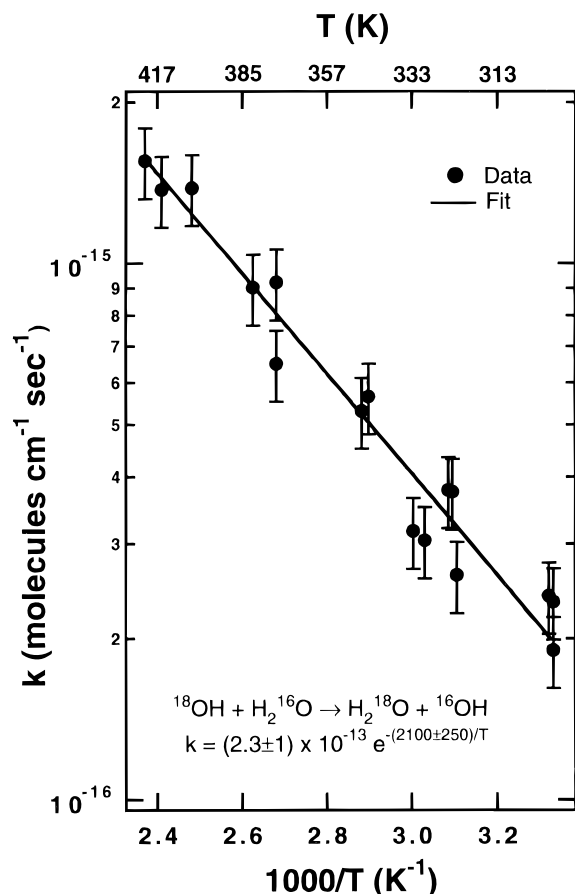
Kinetics of Hydroxyl Radical with Water

J. Phys. Chem. A, Vol. 101, No. 8, 1997 **1497**

Figure 3. Arrhenius plot. Measured rate constants for $^{18}OH + H_2^{16}O \rightarrow H_2^{18}O + {^{16}OH}$ at various temperatures from 300 to 420 K in a log scale are plotted against $1000/T$. The line is the Arrhenius fit.

decays without any interference from secondary reactions are observed subsequent to addition of excess H_2O. The average of five experiments under various flow conditions yields a bimolecular rate constant of $(3 \pm 1.0) \times 10^{-16}$ cm³ molecule⁻¹ s⁻¹ for reaction 3 at 300 K. In addition, we observed the OD production from the reaction

$$OH + D_2O \rightarrow HOD + OD \qquad (5)$$
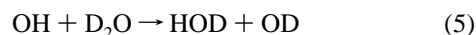
which allows us to put an upper limit of 5×10^{-17} cm³ molecule⁻¹ s⁻¹ for the rate of reaction 5 at 300 K.

III. Implications of Measurements

A. Models of Hydrogen Abstractions. *Reaction Mechanism.* We have demonstrated that reactions 2 and 3 are very slow at room temperature. A large activation energy of 4.2 ± 0.5 kcal mol⁻¹ is observed for reaction 2. In addition, we can place an upper limit on the room temperature rate for reaction 1 of 1×10^{-17} cm³ molecule⁻¹ s⁻¹, indicating either that complex formation is slow or that rapid complex decomposition has established an OH steady state on a time scale shorter than we can resolve (~ 0.01 s).

Substituting OD for OH increases the average rate ($k_3/k_2 = 1.36$) because the reduction of zero-point energy (ZPE) caused by the increased mass is larger at the tight transition state than for the reactants. Three additional asymmetric modes are altered at the DO–H–OH transition state (OD stretch, DOH bend, OD torsion), while only one mode is modified in the reactants (OD stretch). On the other hand, substituting D_2O for H_2O decreases the average rate substantially. While the ZPE of the DO–H–OH and HO–D–OD transition states should be similar, because the modes involving the central atom have

much smaller isotope shifts, the ZPE of the reactants OH and D_2O is much lower than that for OD and H_2O. From the aforementioned one stretch and one bend, we predict $k_5/k_3 > 0.04$, using reagent ZPE shifts only and an even smaller limit when tunneling is included. This is consistent with our observation that reaction 5 is much slower than reaction 3 ($k_5/k_3 < 0.17$).

The large activation energy of reaction 2 is not sufficient to establish a direct mechanism. In fact, the observed preexponentials for reactions 2 and 3 are a factor of 4 lower than values typical of direct H abstractions,[17] indicating an indirect pathway. The origin of this suppression of the preexponential factor can be traced to two electronic properties; the large dipole moments of the reactants and frontier orbital (FMO) stabilization involving electron delocalization from the highest occupied lone pair orbitals in H_2O (HOMO) to the singly occupied π_O orbital in OH (SOMO). These anisotropic long-range forces steer the polar reactants into the complex (Figure 1), whose geometry is unfavorable for H abstraction. The internal rotation of OH in the complex, which is required to establish overlap of the reactive molecular orbitals (RMOs which are π_O in OH, $\sigma_{O–H}$ in H_2O) at the transition state (Figure 1), provides an entropic constraint to the reaction probability. This rotation destroys the dipole–dipole stabilization of the complex, creating a repulsive wall for the reagents to reach the transition state. The complex therefore does play an important role in determining the rate constant, even though it escapes direct observation.

Reactivity Trends. Along the series of H abstractions by OH from saturated hydrocarbons, the reagent frontier orbitals (electron delocalization from the bonding $\sigma_{O–H}$ in the hydrocarbons to the singly occupied π_O in OH) transform smoothly to the transition state and product electronic configuration. Since the FMOs are the RMOs, a simple trend of lower activation energy with increasing ionization potential of the hydrocarbons (first IP of $\sigma_{O–H}$ orbital) is observed.[12] However, for molecules with diffuse lone pairs (like H_2O, NH_3, HNO_3) as the outermost electrons, the OH radical has to interact with the inner $\sigma_{O–H}$ pairs (RMO) in order to undergo H abstraction.[17] (The ionization potential of the outer lone pairs is lower than that of the inner $\sigma_{O–H}$ pairs in these molecules.) Since the FMOs and RMOs are distinct, such reactions are likely to proceed indirectly, as was discussed for the title reaction earlier. Furthermore, both reagent RMO and FMO mediated charge transfer stabilizations will govern reactivity. Therefore, properties of the RMO, its ionization potential and phase relation to the FMO, will have to be included in developing a reactivity index for such reactions.

Another approach to predicting reactivity trends is to examine a series of reactions at the same level of *ab initio* theory and then to make corrections for the known deficiencies of the theory, using measured rate parameters as constraints. To apply this approach to H atom abstractions, we have located the symmetric HO–H–OH saddle point by optimizing the geometry at the UHF/6-31G** theoretical level.[18] The transition state is very tight and lies 19.2 kcal/mol above the reactants at the UMP2 level. The geometry depicted in Figure 1 has the active O–H–O bonds almost collinear (178.1°), and they are stretched by 0.25 Å relative to the O–H bond H_2O. The terminal OH bonds are unperturbed. The theoretical overestimation of the barrier is well-known.[19] It results from basis set limitations, incomplete treatment of electron correlation by the UMP2 method, and the occurrence of H atom tunneling. However, if we assume that the calculated barriers are proportional to the real barriers, we can scale trends in computed UMP2/UHF// 6-31G** barrier heights with observed activation energies for numerous H abstraction reactions. This semiempirical correla-
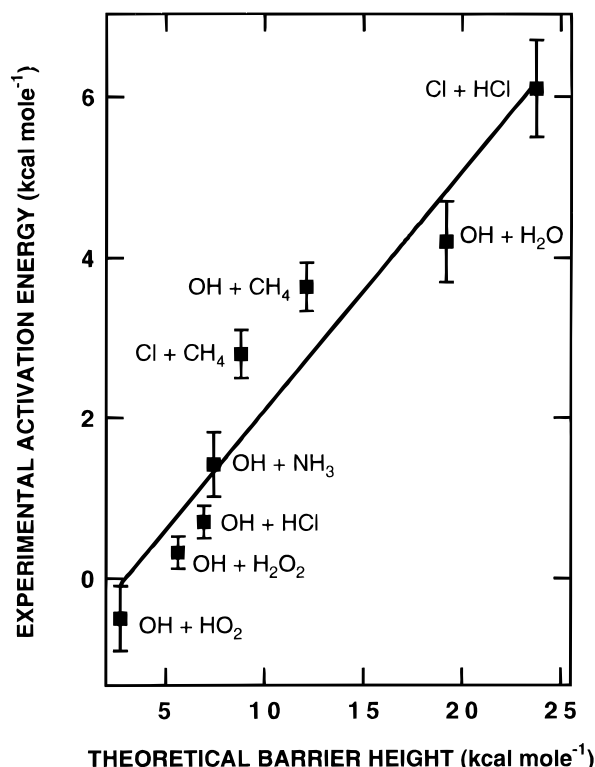
Figure 4. Experimental activation energy vs theoretical barrier height. Measured activation energies (E_{Expt}) are plotted against the theoretical barrier heights (E_{Theory}) for various H abstraction reactions, as indicated. The *ab initio* barriers are at the UMP2/UHF//6-31G** level of theory and include zero-point energy effects. A linear least-squares analysis predicts a barrier of 5 ± 1 kcal mol^{-1} for OH + H$_2$O. Our experimental value of 4.2 ± 0.5 kcal mol^{-1} is in agreement with this. The line represents the linear least-squares fit ($E_{Expt} = -0.9 + 0.3E_{Theory}$) and captures the shown activation energies to within ± 1 kcal mol^{-1}.

tion is shown in Figure 4. It predicts an experimental activation energy of 5 ± 1 kcal/mol for the isotope exchange reactions 1 and 2. Our measured activation energy of 4.2 ± 0.5 kcal mol^{-1} for reaction 2 is in accord with the semiempirical trends.

We now combine our results with published results of other isotope exchange reactions to test the predictive power of thermodynamic models of reactivity. As illustrated in Figure 5, Marcus theory[2] describes the reaction barrier, E_{AB}, of a reaction

$$A + H-B \rightarrow A-H + B \qquad (6)$$
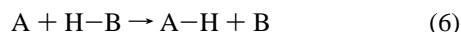
in terms of a purely electronic intrinsic barrier that is displaced by an amount related to the enthalpy (ΔH) of the reaction. The intrinsic barrier, E^0, is defined to be the mean of the barriers (E_{AA} and E_{BB}) for the following thermoneutral identity reactions,

$$A + H-A \rightarrow A-H + A \qquad (7)$$

$$B + H-B \rightarrow B-H + B \qquad (8)$$
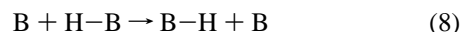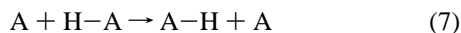
The transition state for reaction 6 is assumed to lie at the intersection of the two parabolic surfaces that represent the energies of the bonds being broken (B−H) and formed (A−H) within the harmonic approximation. The activation energy of reaction 6, E_{AB}, is then predicted by the Marcus equation,

$$E_{AB} = E^0\{1 + [\Delta H/(4E^0)]\}^2 \qquad (9)$$

Marcus theory has been successfully applied to oxidation−reduction reactions in solution, where it is appropriate because the transferred electron is only loosely coupled to the nuclear

motions during reaction.[20] In contrast, at the transition state for H abstraction reactions the electron that is transferred with the H atom remains tightly coupled to the terminal atoms (A and B). While a published study supports the ability of eq 9 to capture reactivity trends among H abstraction reactions,[2] the evidence presented there suffers from the use of theoretical estimates (bond-energy bond-order method[21]) for the intrinsic barriers. We identify an experimentally characterized reaction set where A and B are H,[22] Cl,[23,24] OH, or CH$_3$[25,26] and predict the activation barriers for the six independent gas phase H abstraction reactions (like reaction 8) using the four available isotope exchange measurements of intrinsic activation energies using eq 9. These predictions, when compared with experimental data (Table 1), reveal that Marcus theory succeeds in only two of the six cases. This breakdown indicates that strong electronic interactions between reagents and tunneling probabilities at the transition state are important in determining reactivity and cannot be treated as constants along the reaction series. We affirm Marcus's apprehension concerning the extension to atom transfer reactions of his theory, which was developed for electron transfer processes.[20]

B. Atmospheric Models. *Paleoclimate Inversion Schemes.* The measurement of the isotopic composition (H$_2^{18}$O, HOD, HOH) of ancient water is used to reconstruct paleoclimate temperatures.[27] The basis of this inversion method is the observed linear relationship between water isotope content and surface air temperatures for present-day climates.[28] Paleotemperatures are inferred from water isotope measurements by incorporating the Rayleigh distillation scheme[29] in general circulation models.[28] Each condensation event depletes an air parcel of heavier isotopes since their equilibrium vapor pressures are lower than the lighter H$_2^{16}$O. However, these inversion algorithms neglect possible fractionation of water isotopes from gas phase photochemical processes. Of these, the most likely are reactions with OH, the predominant oxidant in the atmosphere,

$$HO + H^{18}OH \rightarrow HOH + {}^{18}OH \qquad (10)$$

$$HO + HOD \rightarrow HOH + OD \qquad (11)$$

We use our exchange rate measurements, together with contemporary global average OH abundance of 9.7×10^5 molecules cm^{-3},[30] to assess this potential complication. Using the rate constants for reactions 2 and 3 as surrogates for reactions 10 and 11, we predict the time constant for OH-induced isotope exchange of H^{18}OH and HOD to be of order 350 and 175 years, respectively. This is more than 3 orders of magnitude slower than fractionation from condensation, which occurs on the time scale of weeks. This validates the omission of kinetic fractionation of water isotopes in the derivation of paleotemperatures.

Stratospheric Water. In the stratosphere, water regulates the abundance of odd hydrogen species, which in turn dominate catalytic ozone losses at low[31] and high altitudes.[32] Water also controls the frequency and extent of polar stratospheric clouds, which activate chlorine, triggering the rapid and large ozone loss episodes above Antarctica.[33] Stratospheric water has two sources: (1) direct injection of tropospheric water by deep convection in the tropics and (2) photochemical production principally by the oxidation of CH$_4$ by OH.[34] Information on directly injected water flux will also provide an invaluable constraint to the mechanism of stratosphere−troposphere exchange.[35] Despite the importance of stratospheric water, our knowledge of the relative size and global distribution of these sources is limited.

Kinetics of Hydroxyl Radical with Water

J. Phys. Chem. A, Vol. 101, No. 8, 1997 **1499**

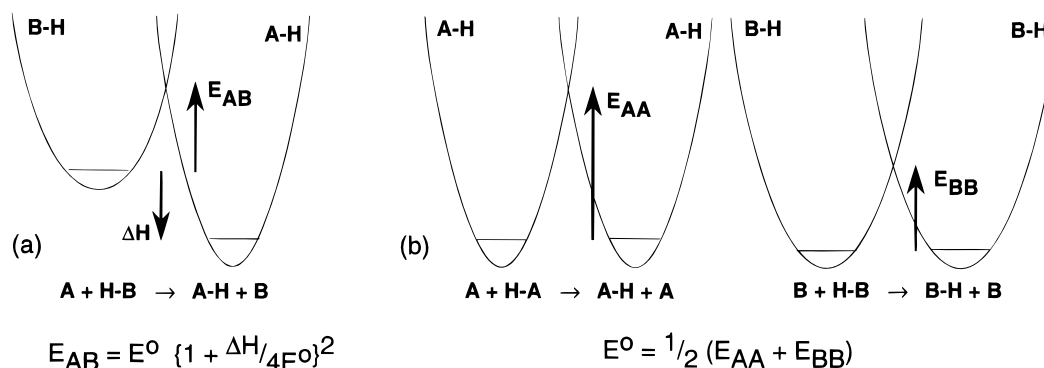$$E_{AB} = E^0 \left\{1 + \frac{\Delta H}{4E^0}\right\}^2 \qquad E^0 = \frac{1}{2}(E_{AA} + E_{BB})$$

Figure 5. Marcus theory for H abstraction reactions. Simplified potential energy surfaces for H abstraction reactions. The barrier is assumed to lie at the intersection of the two parabolic surfaces representing the energies of the bonds being broken and formed, within the harmonic approximation. This framework leads to the Marcus equation that relates the barrier height, E_{AB}, to the reaction energetics, ΔH, of the reaction $A + H-B \rightarrow A-H + B$. This is illustrated for an exoergic reaction (negative ΔH) in (a). The theory contains as a free parameter the purely electronic "intrinsic barrier", E^0, which is defined as the mean of the barriers of the two identity reactions shown in (b). By using measured activation energies of isotope exchange reactions to constrain the "intrinsic barriers", we empirically test the predictive ability of Marcus theory for H abstraction reactions.

TABLE 1: Comparison of Activation Energies Predicted by Marcus Theory with Measurements[a]

A	B			
	H	Cl	OH	CH$_3$
H	9.9*			
Cl	bad			bad
	4.6* (7.7)	5.5*		2.8* (10.8)
OH	bad	bad		good
	4.0* (1.5)	0.7* (0.1)	4.2*	3.6* (3.4)
CH$_3$	good			
	10.9* (11.4)			14.1*

[a] Activation energies in kcal mol^{-1} for the H abstraction reactions $A + H-B \rightarrow A-H + B$. Diagonal elements are from measurements of isotope exchange reactions. The off-diagonal elements show observed and predicted activation energies for H abstraction reactions. Experimental activation energies[14,41] are indicated by an asterisk. Activation energies for H abstractions calculated by the Marcus relation (eq 9) are shown in parentheses. This prediction uses experimental values for ΔH and the mean of the two experimental intrinsic barriers (the two diagonal elements that intersect with the reaction in the table). The agreement is bad for four reactions (Cl + H$_2$, Cl + CH$_4$, OH + H$_2$, OH + HCl) and good for two reactions (OH + CH$_4$, CH$_3$ + H$_2$) as indicated. Microscopic reversibility relates the six empty elements to their symmetric counterparts by thermochemistry.

Isotopic composition of stratospheric water can be useful in delineating the strength of the two sources. Water originating from the troposphere will be depleted in the heavy isotopes (^{18}O and D) by condensation and should dominate in the lower tropical stratosphere. In contrast, simplified isotopic models[36,37] indicate that water produced photochemically in the upper stratosphere should be enriched in the heavier isotopes. While CH$_3$D oxidation should result in a large enrichment in HOD,[36] photochemically produced H^{18}OH is expected to carry only a small fraction of the ^{18}O enrichment present in stratospheric ozone.[37] Observations of water isotopes in the stratosphere qualitatively confirm these predictions.[38] In fact, recent analysis of satellite observations (atmospheric trace molecule spectroscopy: (ATMOS)) of both CH$_3$D and HOD in the stratosphere quantifies these isotope effects and constrains the stratospheric odd hydrogen budget.[39] ATMOS data on HOD also provide evidence that tropical deep convection plays a key role in tropospheric−stratospheric exchange.[40] The potential of using the distinct isotopic signatures to quantitatively separate the two stratospheric water sources exists. Unfortunately, kinetically resolved stratospheric photochemical models necessary to analyze the isotopic data are in their infancy. Our measurements of the slow isotope exchange of OH with water also demonstrate that kinetic fractionation of water by OH can be excluded in such models.

IV. Conclusion

We have observed slow isotope exchange rates of hydroxyl radicals with water. The HO−H$_2$O complex well depth is not large enough to cause rapid isotopic scrambling. However, a suppressed preexponential factor indicates that the entrance channel adduct poses an entropic constraint for the isotope exchange reactions. Our time resolution is too long to observe the complex directly. Simple ZPE shifts of the transition state energy relative to energy of the reactants qualitatively explain the kinetic isotope effects we observe. We show that thermodynamic reactivity models are unreliable. Semiempirical trends between theoretical barrier heights and observed activation energies that include electronic effects at the transition state provide a better prescription for predicting reactivity.

Inversion schemes that derive paleoclimate temperatures from the isotopic composition of ancient water, as well as models analyzing the abundance of water isotopes in the stratosphere, ignore the isotope exchange of water with OH. Our measurement of the slow rate of these isotope exchange reactions validates this assumption.

References and Notes

(1) Fukui, K. *Theory of Orientation and Stereoselection*; Springer-Verlag: Heidelberg, 1975.

(2) Marcus, R. A. *J. Phys. Chem.* **1968**, *72*, 891.

(3) Xie, Y.; Schaefer, H. F. *J. Chem. Phys.* **1993**, *98*, 8829.

(4) Margitan, J. J.; Kaufman, F.; Anderson, J. G. *Chem. Phys. Lett.* **1975**, *34*, 485.

(5) Dransfeld, P.; Lukacs, J.; Wagner, H. G. *Z. Naturforsch., A.: Phys., Phys. Chem., Kosmophys.* **1986**, *41*, 1283.

(6) Greenblatt, G.; Howard, C. J. *J. Phys. Chem.* **1989**, *93*, 1035.

(7) Mohrschladt, R.; Dubey, M. K.; Donahue, N. M.; Anderson, J. G. Manuscript in preparation.

(8) Vaghjiani, G. L.; Ravishankara, A. R.; Cohen, N. *J. Phys. Chem.* **1989**, *93*, 7833.

(9) Gupta, M.; Tyler, S.; Cicerone, R. *J. Geophys. Res.* **1996**, *101*, 22923.

(10) Brenninkmeijer, C. A. M.; Muller, R.; Crutzen, P. J.; Lowe, D. C.; Manning, M. R.; Sparks, R. J.; Velthoven, P. F. J. v. *Geophys. Res. Lett.* **1996**, *23*, 2125.

(11) Butler, J. E.; Talley, L. D.; Smith, G. K.; Lin, M. C. *J. Chem. Phys.* **1981**, *74*, 4501.

(12) Abbatt, J. P. D.; Demerjian, K. L.; Anderson, J. G. *J. Phys. Chem.* **1990**, *94*, 4566.

(13) Donahue, N. M.; Clarke, J. S.; Demerjian, K. L.; Anderson, J. G. *J. Phys. Chem.* **1996**, *100*, 5821.

(14) DeMore, W. B.; Sander, S. P.; Howard, C. J.; Ravishankara, A. R.; Golden, D. M.; Kolb, C. E.; Hampson, R. F.; Kurylo, M. J.; Molina,

M. J. *Chemical Kinetics and Photochemical Data for Use in Stratospheric Modeling*; NASA/JPL: 1994.

(15) Cantrell, C. Private communication, 1996.

(16) Mohrschladt, R.; Dubey, M. K.; Donahue, N. M.; Anderson, J. G. Manuscript in preparation.

(17) Dubey, M. K. Ph. D. Thesis, Harvard University, 1994.

(18) Frisch, M. J.; Trucks, G. M.; Head-Gordon, M.; Gill, P. M. W.; Wong, M. W.; Foresman, J. B.; Johnson, B. G.; Schlegel, H. B.; Robb, M. A.; Replogle, E. R.; Gompters, R.; Andres, J. L.; Raghavachari, K.; Binkley, J. S.; Gonzalez, C.; Martin, R. L.; Fox, D. J.; DeFrees, D. J.; Baker, J.; Stewart, J. J. P.; Pople, J. A. *GAUSSIAN92/DFT*; Gaussian Inc.: Pittsburgh PA, 1991.

(19) Toohey, D. W.; Anderson, J. G. *J. Phys. Chem.* **1989**, *93*, 1049.

(20) Marcus, R. A. *Angew. Chem., Int. Ed. Engl.* **1993**, *32*, 1111.

(21) Johnston, H. S.; Parr, C. *J. Am. Chem. Soc.* **1963**, *85*, 2544.

(22) Michael, J. V.; Fisher, J. R. *J. Phys. Chem.* **1990**, *94*, 3318.

(23) Klein, F. S.; Persky, A.; Weston, R. E. *J. Chem. Phys.* **1964**, *41*, 1799.

(24) Garrett, B. C.; Truhlar, D. G.; Wagner, A. F.; Dunning, T. H. *J. Chem. Phys.* **1983**, *78*, 4400.

(25) Dainton, F. S.; Ivin, K. J.; Wilkinson, F. *Trans. Faraday Soc.* **1957**, *53*, 1204.

(26) Creak, G. A.; Dainton, F. S.; Ivin, K. J. *Trans. Faraday Soc.* **1962**, *58*, 326.

(27) Jouzel, J.; Lorius, C.; Petit, J. R.; Genthon, C.; Barkov, N. I.; Kotlyakov, V. M.; Petrov, V. M. *Nature* **1987**, *329*, 403.

(28) Koster, R. D.; Valpine, D. P. d.; Jouzel, J. *Geophys. Res. Lett.* **1993**, *20*, 2215.

(29) Dansgaard, W. *Tellus* **1964**, *16*, 436.

(30) Prinn, R. G.; Weiss, R. F.; Miller, B. R.; Huang, J.; Alyea, F. N.; Cunnold, D. M.; Fraser, P. J.; Hartley, D. E.; Simmonds, P. G. *Science* **1995**, *269*, 187.

(31) Wennberg, P. O.; Cohen, R. C.; Stimpfle, R. M.; Koplow, J. P.; Anderson, J. G.; Salawitch, R. J.; Fahey, D. W.; Woodridge, E. L.; Keim, E. R.; Gao, R. S.; Webster, C. R.; May, R. D.; Toohey, D. W.; Avallone, L. M.; Proffitt, M. H.; Loewenstein, M.; Podolske, J. R.; Chan, K. R.; Wofsy, S. C. *Science* **1994**, *266*, 398.

(32) Jucks, K. W.; Johnson, D. G.; Chance, K. V.; Traub, W. A.; Salawitch, R. J.; Stachnik, R. A. *J. Geophys. Res.* **1996**, *101*, 28785.

(33) Albritton, D. A.; Watson, R. T.; Auchamp, P. J. *Scientific Assessment of Ozone Depletion: 1994*; World Metereological Organization Report No. 37, 1996.

(34) Remsberg, E. E.; Bhatt, P. P.; III, J. M. R. *J. Geophys. Res.* **1996**, *101*, 6749.

(35) Holton, J. R.; Hayes, P. H.; McIntyre, M. E.; Douglas, A. R.; Pfister, L. *Rev. Geophys.* **1995**, *33*, 403.

(36) Kaye, J. A. *Rev. Geophys.* **1987**, *25*, 1609.

(37) Kaye, J. A. *J. Atmos. Chem.* **1990**, *10*, 39.

(38) Rinsland, C. P.; Gunson, M. R.; Foster, J. C.; Toth, R. A.; Farmer, C. B.; Zander, R. *J. Geophys. Res.* **1991**, *96*, 1057.

(39) Irion, F. W.; Moyer, E. J.; Gunson, M. R.; Rinsland, C. P.; Yung, Y. L.; Michelson, H. A.; Salawitch, R. J.; Chang, A. Y.; Newchurch, M. J.; Abbas, M. M.; Abrams, M. C.; Zander, R. *Geophys. Res. Lett.* **1996**, *23*, 2381.

(40) Moyer, E. J.; Irion, F. W.; Yung, Y. Y.; Gunson, M. R. *Geophys. Res. Lett.* **1996**, *23*, 2385.

(41) Kerr, J. A.; Moss, S. J. *CRC Handbook of Bimolecular and Termolecular Gas Reactions*; CRC Press: Boca Raton, FL, 1981.